Tunable Donor Aggregation Dominance in Ternary Matrix of All-polymer Blends with Improved Efficiency and Stability

Ruijie Ma[1], Hongxiang Li[2], Top Archie Dela Peña[3,5], Xiyun Xie[1], Patrick Wai-Keung Fong[1], Qi Wei[3], Cenqi Yan[2], Jiaying Wu[5], Pei Cheng[2], Mingjie Li[3], Gang Li[1,4]*

[1] Department of Electronic and Information Engineering, Research Institute for Smart Energy (RISE), Guangdong-Hong Kong-Macao (GHM) Joint Laboratory for Photonic-Thermal-Electrical Energy Materials and Devices, The Hong Kong Polytechnic University, Hung Hom, Kowloon, Hong Kong, 999077, China

Email: gang.w.li@polyu.edu.hk

[2] College of Polymer Science and Engineering, State Key Laboratory of Polymer Materials Engineering, Sichuan University, Chengdu, China

[3] Department of Applied Physics, The Hong Kong Polytechnic University, Hong Kong, China

[4] The Hong Kong Polytechnic University Shenzhen Research Institute, Shenzhen, 518057, China

[5] Advanced Materials Thrust, Function Hub, The Hong Kong University of Science and Technology, Nansha, Guangzhou, China

This article has been accepted for publication and undergone full peer review but has not been through the copyediting, typesetting, pagination and proofreading process, which may lead to differences between this version and the Version of Record. Please cite this article as doi: 10.1002/adma.202304632.

Abstract

Using two structurally similar polymer acceptors in constructing high-efficiency ternary all-polymer solar cells is a widely acknowledged strategy. However, the focus thus far has not been on how polymer acceptor(s) tune the aggregation of polymer donors, thus furthering film morphology and device performance (efficiency and stability). Herein, we report that matching the celebrity acceptor PY-IT and donor PBQx-TCl results in enhanced *H*-aggregation in PBQx-TCl, which can be finely tuned by controlling the amount of the second acceptor PY-IV. Consequently, the efficiency-optimized PY-IV weight ratio (0.2/1.2) leads to state-of-the-art power conversion efficiency of 18.81%, wherein light-illuminated operational stability is also enhanced along with well-protected thermal stability. Such enhancements in the efficiency and operational and thermal stabilities of solar cells can be attributed to morphology optimization and desired glass transition temperature of the target active layer based on comprehensive characterization. In addition to being a high-power conversion efficiency case for all-polymer solar cells, these enhancements are also a successful attempt for using combined acceptors to tune donor aggregation toward optimal morphology, which provides a theoretical basis for the construction of other types of organic photovoltaics beyond all-polymer solar cells.

Keywords: donor aggregation, morphology modulation, all-polymer solar cells, power conversion efficiency, stability

Introduction

The photovoltaic performance, that is, the power conversion efficiency (PCE) of all-polymer solar cells (all-PSCs), has been improved via polymerized small molecular

acceptor (PSMA) synthesis and accompanied device engineering, thereby generating operationally and mechanically stable solar cells.[1-10] The ternary or multi-component blending strategy using new or reported materials has been the most powerful method in boosting organic solar cells, and researchers have achieved various over 18% efficiency cases for all-PSCs.[11-20] Elucidation of the working mechanism of high-efficiency all-PSC systems is still lacking, and a comprehensive revelation of the interaction among donor(s), acceptor(s), and processing solvent(s) is of great importance to both academic and industrial researchers.[21-23]

Apart from small molecular acceptor (SMA) materials, newly developed PSMAs have a stronger tendency to aggregate than that exhibited by other polymer materials, suggesting that the donor polymers could be tuned to a relatively greater degree to modulate their pre-aggregation behavior. This possibility indicates that ternary all-PSC systems, especially those with two PSMAs, may offer new physical insights different from those in blends with two SMAs. Once the ternary matrix working mechanism is well addressed, minimizing the efficiency gap between ternary all-PSC systems and cutting-edge organic photovoltaic (OPV) devices will be feasible.[24-33]

Herein, we have focused on three materials and one phenomenon in their ternary blends, that is, three reported efficient OPV active materials—PBQx-TCl as donor and PY-IT and PY-IV as acceptors—that form the ternary system.[34-37] Within this system, PBQx-TCl exhibits strong *H*-aggregation when PY-IT content is high and intense *J*-aggregation when PY-IV dominates the acceptor part. The most optimal PCE is achieved using a minor PY-IV incorporated system, wherein *H*-aggregation is well preserved, with high open-circuit voltage (V_{OC}) and red-shifted absorption profile for improved short-circuit current density (J_{SC}). Meanwhile, the high fill factor (*FF*) value is due to the simultaneously well-modulated phase segregation, molecular packing features, and suppressed recombination dynamics.

Furthermore, the process of morphology determination (spin coating and thermal annealing) is screened by *in-situ* reflectance spectroscopy tracing, which aids in determining the tunability of donor aggregation. Compared with PY-IV, PY-IT delays and decelerates the second stage of PBQx-TCl aggregation. However, PY-IT aggregation also follows the same protocol as that for the donor. In addition, thermal annealing treatment enhances PBQx-TCl aggregation more than that of the acceptor, further proving that the fundamental morphology regulating factor herein is the donor phase crystallization and formation. In contrast, the operational stability test enabled by maximal power point (MPP) tracking and thermal stability test (annealing at 100 ℃ in N_2 atmosphere) results show that modulated morphology and desired glass transition temperature (T_g) also contribute to improved lifetime in different degradation conditions. With state-of-the-art photovoltaic performances and elucidation of the underlying mechanisms, this study presents improved instructive ideas for using all-PSCs in the future.

Results and Discussion

Figure 1a presents the chemical structures of the materials, and their availability is elaborated in ***Supporting Information***. The basic properties of materials were first investigated through ultraviolet–visible (UV–Vis) absorption measurements on a neat donor film and mixed acceptor films with different weight ratios, as presented in **Figure S1**. The donor PBQx-TCl exhibited two peaks at 538 and 573 nm, with the second peak being higher than the first. For acceptor materials, the position of the principal peak varied from 815 to 821, 822, 829, and 832 nm, alongside the composition rise of PY-IV. All acceptor materials exhibited shoulder peaks at bluer positions than in the other spectral regions, significantly lower than the primary ones. They all have shoulder peaks at bluer positions, significantly lower than the main ones. As for the energy level distribution, according to the literature

reports **(Figure S2)**,[37] there should be a cascaded landscape.[37] The primary molecular packing properties of the materials were evaluated based on grazing incidence wide-angle X-ray scattering (GIWAXS) measurements. The 2D color patterns of PBQx-TCl and PY-IT: PY-IV films with varying ratios are displayed in **Figure S3**. Both donor PBQx-TCl and acceptor PY-IT exhibited a performance-favorable face-on orientation, wherein both in-plane (IP) lamellar and out-of-plane (OOP) π–π stacking peaks were significant. The PY-IV acceptor had a much weaker general crystallinity than that of PY-IT; thus, the acceptor blend films show a negative tendency of crystallinity and orientation with increasing PY-IV content. In addition, the π–π peaks of PBQx-TCl and PY-IT locate closely, which may indicate that their blending could have a mutually assisted strong film crystallinity, and certain additional PY-IV could act as a regulator. Next, the hole transport and electron transport abilities of the polymer donor PBQx-TCl and the two acceptors were evaluated based on the mobility values (μ_h and μ_e), which were calculated using the space charge limited current method. Based on the device results plotted in **Figure S4**, PBQx-TCl contained a μ_h of 1.13×10^{-3} $cm^2 \cdot V^{-1} \cdot s^{-1}$, whereas PY-IT: PY-IV combinations with increasing weight ratios exhibited μ_e values of 1.15×10^{-3}, 1.26×10^{-3}, 1.21×10^{-3}, 1.20×10^{-3}, and 1.17×10^{-3} $cm^2 \cdot V^{-1} \cdot s^{-1}$ (**Table S1**). As a preliminary conclusion, the three materials have similar charge mobilities, though they differ significantly in their crystallinity.

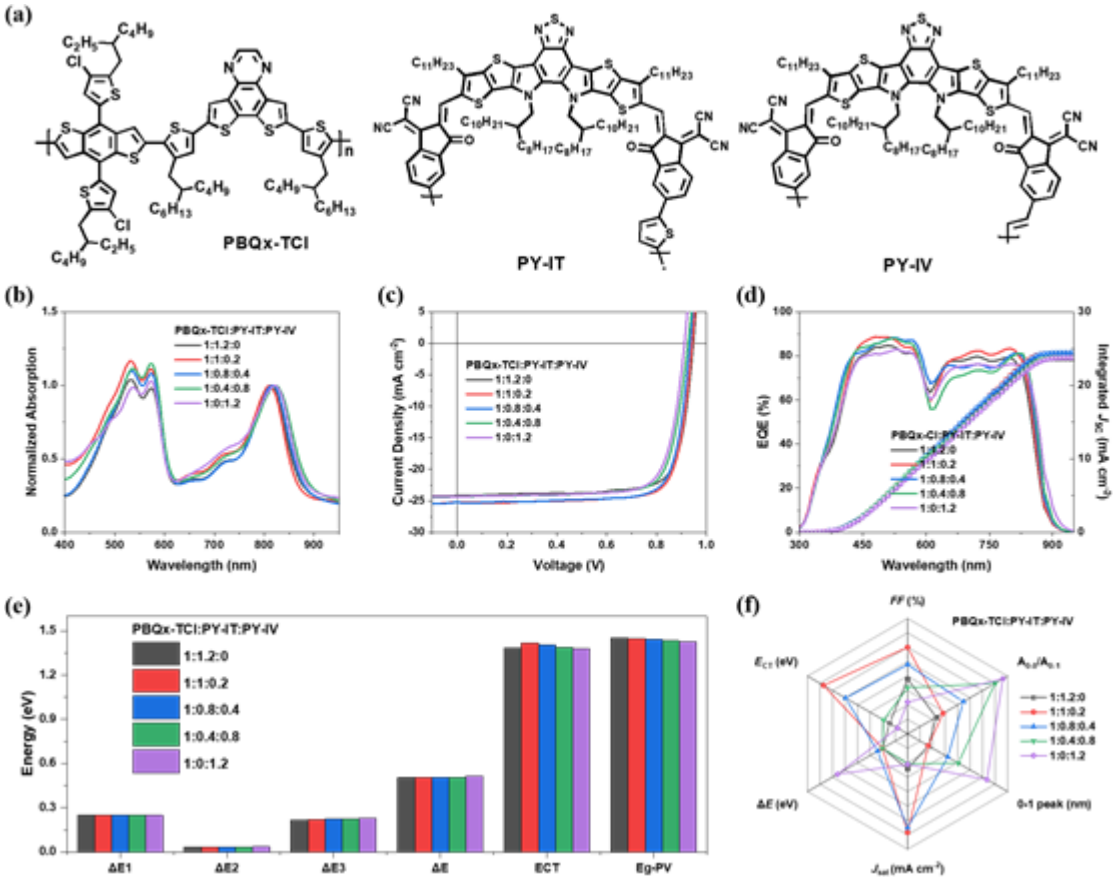

Figure 1. (a) Chemical structures. (b) Acceptor-normalized absorbance for blend films. (c) Current density vs. voltage (*J*–*V*) characteristics. (d) External quantum efficiency (EQE) spectra and integrated short-circuit current density (J_{SC}) values. (e) Calculated parameters for bandgap, charge transfer (CT) state, and energy loss. (f) Correlation among critical factors.

Table 1. Device performances.

PBQx-TCl: PY-IT: PY-IV	V_{OC} (V)	J_{SC} (mA · cm^{-2})	*FF* (%)	PCE (%)
1:1.2:0	0.947	24.18/23.62	77.9	17.84 (17.55 ± 0.27)
1:1:0.2	0.943	25.25/24.43	79.0	18.81 (18.58 ±

				0.23)
1:0.8:0.4	0.935	25.28/24.45	78.4	18.53 (18.21 ± 0.28)
1:0.4:0.8	0.927	24.35/23.77	77.6	17.52 (17.15 ± 0.32)
1:0:1.2	0.912	24.36/23.77	77.1	17.13 (16.85 ± 0.34)

The brackets contain averages and standard errors of PCEs based on 20 devices. Abbreviations: V_{OC}, open-circuit voltage; J_{SC}, short-circuit current density; *FF*, fill factor; PCE, power conversion efficiency.

The properties of blend films were revealed sequentially. Their UV–Vis absorption spectra are illustrate in **Figure 1b**. In PY-IT-dominated films, PBQx-TCl showed higher vibrational peaks of 0-1 than of 0-0 type, differing from its neat film profile. On the contrary, the optical property of PBQx-TCl was retained when PY-IV content was higher than that of PV-IT. Since *H*-aggregated structure leads to enlarged bandgap and *J*-aggregation narrows the bandgap, we can use the rise of 0-1 vibrational peak and the decrease of 0-0 vibrational peak to mark enhanced *H*-aggregation (*J*-aggregation increase reflects as more intense 0-0 peak and weaker 0-1 peak). In addition, the spectral profiles of blend films in long wavelength regions were almost identical to those of acceptor-only films. These results indicate that PBQx-TCl rarely changed the general aggregation behavior of PY-IT and PY-IV, but the aggregation behavior of the donor material was significantly tuned by PY-IT. This result represents a rare example of modulating *H*-aggregation vs. *J*-aggregation of the donor material by varying the acceptor composition. The aggregation transition of PBQx-TCl can be further evidenced based on the results presented in **Figure S1**, as the acceptor peaks in the 400–600 nm range exhibit blue shifting. Thus, once the peak alteration is contributed by

proton absorption by the acceptor, the 0-1 vibrational peak of PBQx-TCl will be higher when PY-IV dominates than when PV-IT dominates the composition. Therefore, this peak of each blend system is supposed to be minimized because of tuned acceptor aggregation, and the change in the intensities of 0-1 and 0-0 peaks for PBQx-TCl can be used as an aggregation inspector.

The photovoltaic performance of this group of all-polymer blends was investigated using a series of devices based on the conventional structure ITO/ PEDOT: PSS/ active layer/PFN-Br-MA/Ag.[38] Their current density vs. voltage (*J*–*V*) characteristics are illustrated in **Figure 1c**, and corresponding parameters are summarized in **Table 1**. The binary all-PSCs of PY-IT and PY-IV achieved over 17% efficiency. Apart from the slightly lower J_{SC} values compared with those of the PBQx-TCl: PY-IV-based device, the PBQx-TCl: PY-IT-based device possessed better V_{OC} and *FF*, contributing to its higher PCE. The ternary blends with 1:0.2 and 0.8:0.4 weight ratios of PY-IT: PY-IV realized improved efficiencies of >18.5%, owing to boosted J_{SC} and *FF* and insignificantly sacrificed V_{OC}. When the proportion of PY-IV in ternary blends adopts the dominant position, the device efficiency drops to 17.52%, closer to that of PY-IV-based binary devices. The external quantum efficiency (EQE) spectra and related J_{SC} integration curves for these cells are depicted in **Figure 1d**. The integrated J_{SC} values are also listed in **Table 1**. The errors were limited to approximately 3% in this work. Furthermore, the redshift response of PY-IV helped to harvest relatively more photons, thus improving J_{SC} for ternary devices.

Relative device physics was studied in order. Based on the photocurrent (J_{ph}) vs. effective voltage (V_{eff}) relationships shown in **Figure S5a** and the corresponding values presented in **Table S2**, the addition of PY-IV promotes saturated current density (J_{sat}) and exciton collection efficiency, which is consistent with changes in J_{SC} and *FF* values. The calculation method is elaborated in ***Supporting Information***, as well. Parallelly, the V_{OC} and J_{SC} curves

across varying light intensities are shown in **Figure S5b** and **S5c**. The fitting slope values for changes in V_{OC} with increasing PY-IV weight ratios were 1.16, 1.08, 1.15, 1.23, and 1.20. Those derived from J_{SC} variation were uniformly 0.99. Thus, the recombination dynamics are partially revealed here, but relatively more insights need to be gained by other characterizations.[39-42]

For a ternary blend construction based on two acceptors, their energy/ charge transfer (CT) characteristics were studied using acceptor-only device fabrication and photoluminescence (PL) measurements (**Figure S6a** and **S6b**).[43-45] Accordingly, no recognizable energy or CT exists between PY-IT and PY-IV. Considering this phenomenon, J_{SC} promotion is mainly due to photo-response edge extension. Furthermore, the charge mobility of blend films is also studied, as demonstrated in **Figure S7** and **Table S3**. The two ternary systems with excellent performance showed relatively more balanced charge transport than in other systems, consistent with their improved *FF* values.

Another critical factor for efficiency improvement can be the non-linearly varied V_{OC}; therefore, we also conducted the energy loss (ΔE) analysis. To serve this purpose, Fourier transform photocurrent spectroscopy, EQE, electroluminescence (EL), and EL–EQE measurements were utilized, accompanied by respective fittings.[46-48] The experimental and fitting results are shown in **Figure 1e** and **Figures S8** and **S9**. A comparison of general energy loss revealed that the main difference in V_{OC} was caused by the larger ΔE values of PY-IV-based cells than of those with high proportions of PY-IT in blends, contributed by concurrent radiative and non-radiative loss. Another substantial issue observed was that ternary systems uniformly showed upshifted CT energy states (E_{CT}) and higher reorganization energy (λ_{RO}) values, which on the one hand, was beneficial to exciton splitting and, on the other hand, helpful in suppressing free charge recombination.[49-50]

After these characterizations, the relationships between donor aggregation mode and device performance and the fundamental device physics parameters could be initially built up, as shown in **Figure 1f**. Morphologically, the *H*-aggregation vs. *J*-aggregation of PBQx-TCl in the active layer could be reflected by the peak position of 0-1 vibrational peak and the value of 0-0 vs. 0-1 peak intensity ratio ($A_{0\text{-}0}/A_{0\text{-}1}$). The ΔE value was negatively related to $A_{0\text{-}0}/A_{0\text{-}1}$, implying that relatively more *J*-aggregates for the donor polymer could drive higher voltage loss. Saturated current density (J_{sat}) and *FF* partially positively correlated with $A_{0\text{-}0}/A_{0\text{-}1}$ and were comparatively more dominated by E_{CT}, indicating that the strong *H*-aggregation of the PY-IT-based binary blend for PBQx-TCl was entirely beneficial for general device performance. However, a finely tuned energy landscape and morphology (caused by the proper addition of PY-IV) realized the optimal PCE.

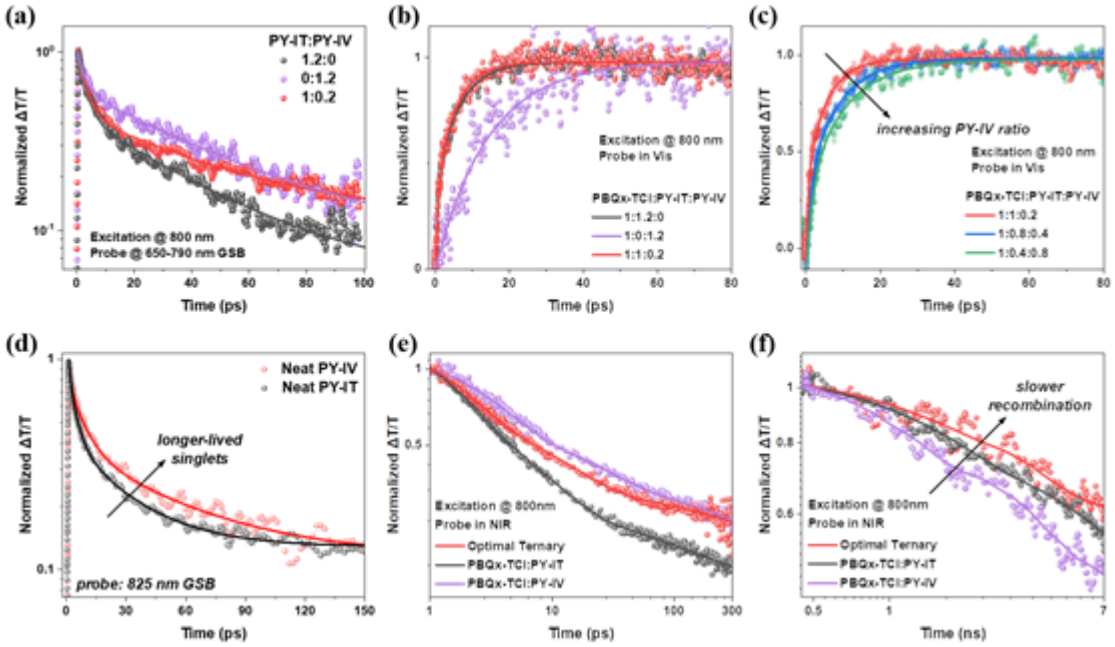

Figure 2. Transient absorption spectra analysis upon selective acceptor excitation. Singlet exciton-based ground-state bleach (GSB) fitting for (a) PY-IT: PY-IV neat and blend films, (b, c) free charge generation in binary and ternary active layers based on hole polarons

photo-bleach signals in the visible region (450–800 nm). (d) Singlet exciton-based GSB fitting for PY-IT: PY-IV neat and blend films, (e) Singlet exciton-based GSB signals in binary and ternary active layers based in the near-infrared (NIR) region (800–1200 nm), and (f) free charge recombination relative to electron-hole polarons. Notably, in (f), the kinetics are normalized at 0.5 ns to represent the recombination behavior of electron polarons as most singlet excitons, initially present after excitation, decay within such a time scale.

The transient absorption spectroscopy test was selected as a powerful tool to elucidate CT and recombination dynamics in binary and ternary blend films. Signals were detected in visible and near-infrared (NIR) regions, as shown in **Figures S10**–**S13**. **Figure 2** shows corresponding fitting lines for CT generation and free-charge recombination kinetics evaluation. In transient absorption spectra, the behavior of singlet excitons in PY-IT: PY-IV blend films was comparable to those in PY-IT neat film at 2–3 ps after excitation. Later, at >20 ps, the singlets in the PY-IT film were evidently quenched; however, and the remaining singlets in the PY-IT: PY-IV blends took a longer time to decay than those in the neat PY-IT film and finally matched the dynamics of PY-IV singlets. This result implies that no significant interaction exists between PY-IT and PY-IV that could generate different exciton behaviors, consistent with the previous conclusion of no clear energy transfer or CT between these two acceptors. The hole transfer kinetics fitted in PBQx-TCl: PY-IT: PY-IV binary and ternary films are presented in **Figure 2b** and **2c** and **Table S4**. The PY-IT-based binary device could generate free charges much faster than those generated by the PY-IV-based binary counterpart, supporting its higher EQE response. The ternary systems with a J_{SC} value of >25 mA·cm^{-2} also demonstrated much faster hole transfer than exhibited by the PY-IV-based binary cells, which further substantiate the enhanced photon harvest using ternary tactics, that is, broadened absorption edge and efficient free charge generation.

These results are further supported by the results of NIR detection and analysis presented in **Figure 2d** and **2e**, as PY-IT dominates the charge generation at an early stage, whereas PY-IV is capable of dominating during later stages owing to longer-lived PY-IV singlet excitons. As displayed in **Figure 2f**, the free charge recombination study is supported by the sub-nanosecond decay of electron-hole polarons, revealing that the ternary target (1:1:0.2 for PBQx-TCl: PY-IT: PY-IV) exhibited the slowest and the PY-IV binary device displayed the fastest recombination rate. This finding is well consistent with the performance of the device. After addressing the concerns related to variations in device physics introduced due to the constructions of the ternary matrix, the core issue regarding the modulation of donor polymer aggregation needs to be further elaborated by a series of morphology characterizations and analyses. In conclusion, the UV–Vis profiles can only provide an initial impression that the morphology is tuned. For gaining further information, relatively more efforts are needed.

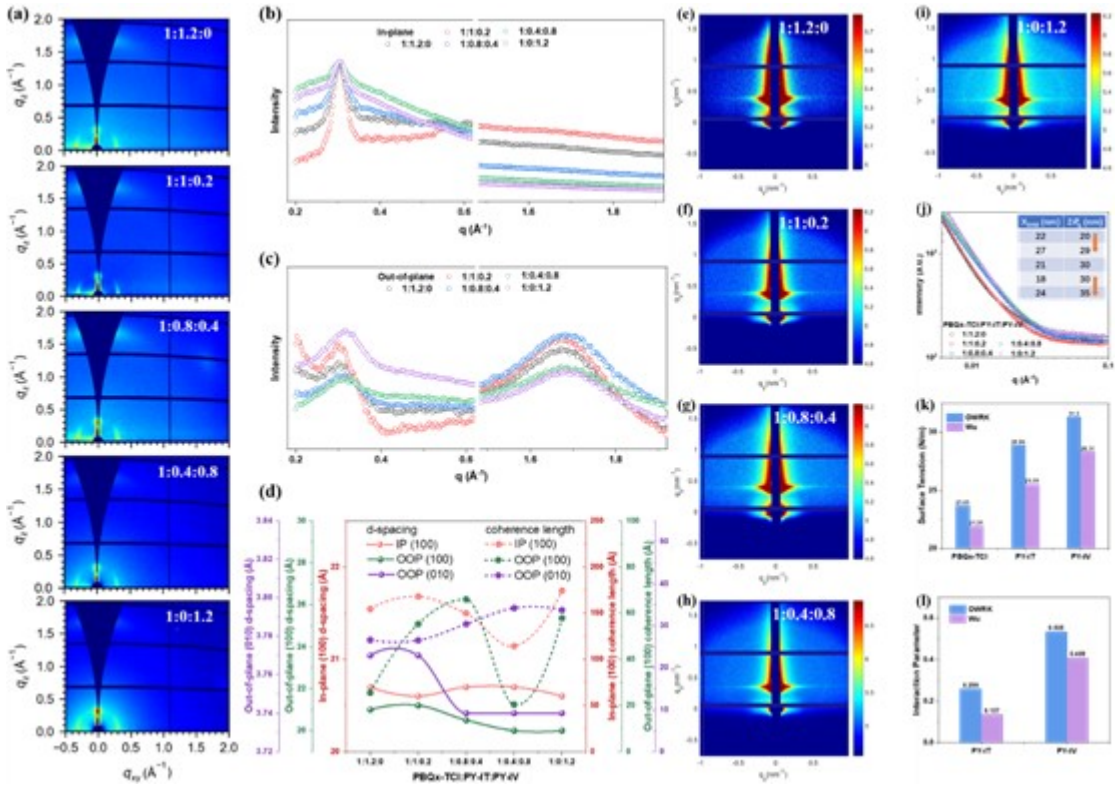

Figure 3. (a) Two-dimensional grazing incidence wide-angle X-ray scattering (2D-GIWAXS) patterns and corresponding (b) in-plane (IP) and (c) out-of-plane (OOP) line-cuts of all active layers. (d) Visualized crystallographic parameters. (e–i) Two-dimensional grazing incidence small angle X-ray scattering (2D-GISAXS) patterns of PBQx-TCl: PY-IT: PY-IV films in all studied ratios. (j) Corresponding in-plane line-cut plots, fitting lines, and derived phase length scales. (k) Surface tension values estimated for donor and acceptor materials and their (l) miscibility analysis based on two algorithms.

GIWAXS experiments were utilized to elucidate the molecular packing and changes in the crystalline properties of blend films. Their 2D patterns are all displayed in **Figure 3a**, with IP and OOP line cuts plotted in **Figure 3b** and **3c**. Using Gaussian fitting, their crystalline parameters, including peak position, d-spacing, and coherence length values, were obtained, as listed in **Table S5** and **S6** and visualized in **Figure 3d**. The general motif PBQx-TCl: PY-IT of binary films represents a typical case of face-on orientation, with intense IP directional (100) peak and OOP directional (010) peak signals. Noticeably, the OOP directional lamellar peak in PY-IT-dominated systems was weak, corresponding to the *H*-aggregation advantaged feature in these films. As for the π–π stacking peaks, PY-IV-dominated systems exhibited lower intensities than those with PY-IT as the main acceptor component. However, the coherence lengths of these films demonstrated a rising tendency when PY-IV content increased. Therefore, the general crystallinity became weaker with increasing PY-IV content, but the crystallite arrangement adopted a relatively more ordered structure within a short distance. Summarizing, adding PY-IV could properly tune the long-distance (lamellar) molecular packing for PBQx-TCl, corresponding to alterations in the heights of 0-0 and 0-1 vibrational peaks. Meanwhile, the charge transport property did not change drastically following variations in the π–π stacking peaks.

In addition, to provide a further evidence of donor aggregation transition from *H*- type to *J*-type, the pole figures of lamellar peaks of blend films are illustrated in **Figure S14**. The

results clearly reveal that donor polymer's long-distance packing turns from a very ordered in-plane mode to a less-oriented motif by increasing the ratio of PY-IV in blend, which are well consistent with absorption spectra generated information. This can be even more easily known by observing **Figure 3a.**

Furthermore, focusing on a larger spatial scale, the phase separation behavior in binary and ternary films was investigated by grazing incidence small angle X-ray scattering (GISAXS) measurements. The 2D patterns are displayed in **Figure 3e**–**3i**, and the IP intensity profiles are plotted in **Figure 3j**. A previously used model was selected for fitting. The obtained intermixing phase length scale (X_{DAB}) and pure phase size ($2R_g$) values are presented in **Figure 3j**.[51-53] Generally, the rise in the length scale of the pure phase with the increase in PY-IV content was apparent, supporting the improved *FF* of the ternary systems. Meanwhile, a larger X_{DAB} value for the optimal ternary film that for the others indicated that the donor/ acceptor interface area for charge dissociation was not compromised, supporting the enhanced J_{SC}.

The contact angles of water and ethylene glycol upon neat films were measured to elucidate the variations in phase separation, and their surface tension values were calculated using Owens–Wendt–Rabel–Kaelble and Wu's methods, respectively.[54] The photographs of the contact angles are put in **Figure S15** with marked angle values. Calculated surface tension values and donor-acceptor miscibility interaction parameters are depicted in **Figure 3k** and **3l**. The higher interaction parameter between PY-IV and PBQx-TCl than between PY-IT and PBQx-TCl corresponds to the better phase separation in the PY-IV-based binary active layer. In addition, by varying the amounts of PY-IV added, the phase separation can be finely tuned towards a desired morphology for concurrently efficient charge separation and transport. All these contact angles were selected based on a stable droplet on target films. The time-resolved variation curves of contact angles are presented in **Figure S16**.

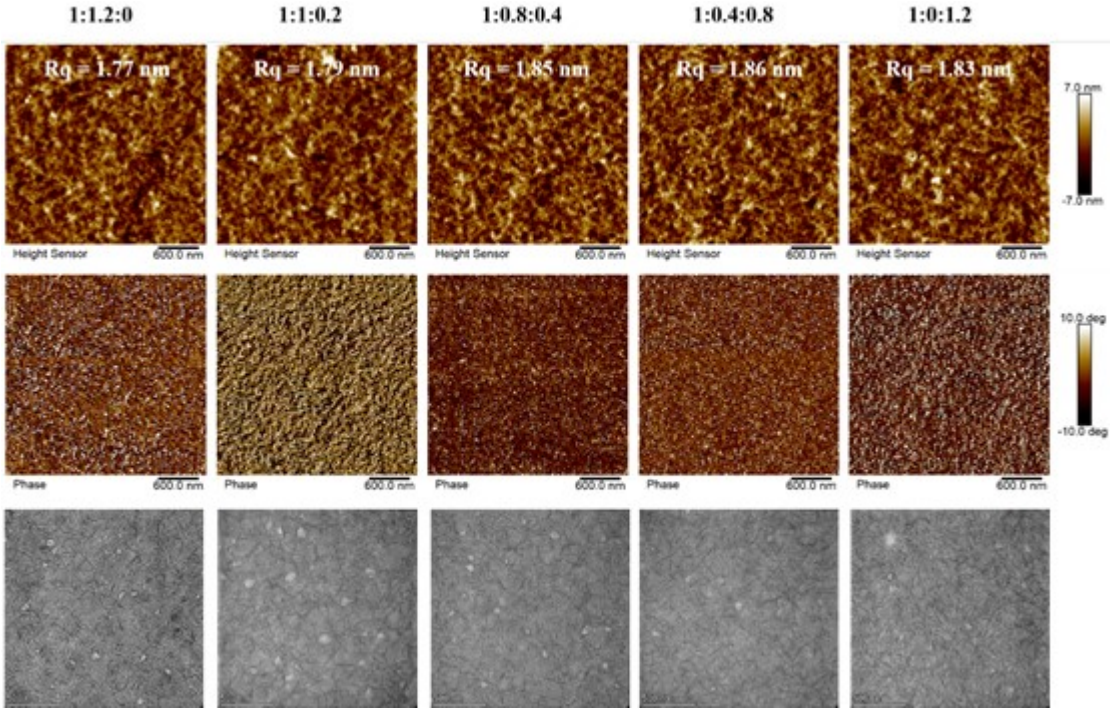

Figure 4. Atomic force microscopy (AFM) height/phase images and transmission electron microscopy (TEM) images of all blend films.

Direct morphology observation was enabled by atomic force microscopy (AFM) and transmission electron microscopy (TEM) technologies. The photographed images are all displayed in **Figure 4**. The variation in surface roughness was excessively insignificant, implying that the top surface contact with the electron transporting layer was not supposed to exert a great impact on charge collection and device performance. However, the AFM phase images could provide relatively more information, that is, the nano-fibrillar networks in the PY-IT-dominated films, particularly the optimal ternary one, were more significant than in the others. These nano-fibrillar networks are acknowledged to be beneficial for efficient charge transport.[25] The TEM images further confirmed the existence of an interpenetrating fibrillar network in all films. The ternary films corresponding to >18% efficiencies exhibited

not only relatively more pronounced network features but also more and larger “white aggregates” than in the others. These agglomerates are suggestive to be the pure phases that could help with suppressing exciton recombination. This phenomenon may also be the result of strong *H*-aggregation of PBQx-TCl in blends.

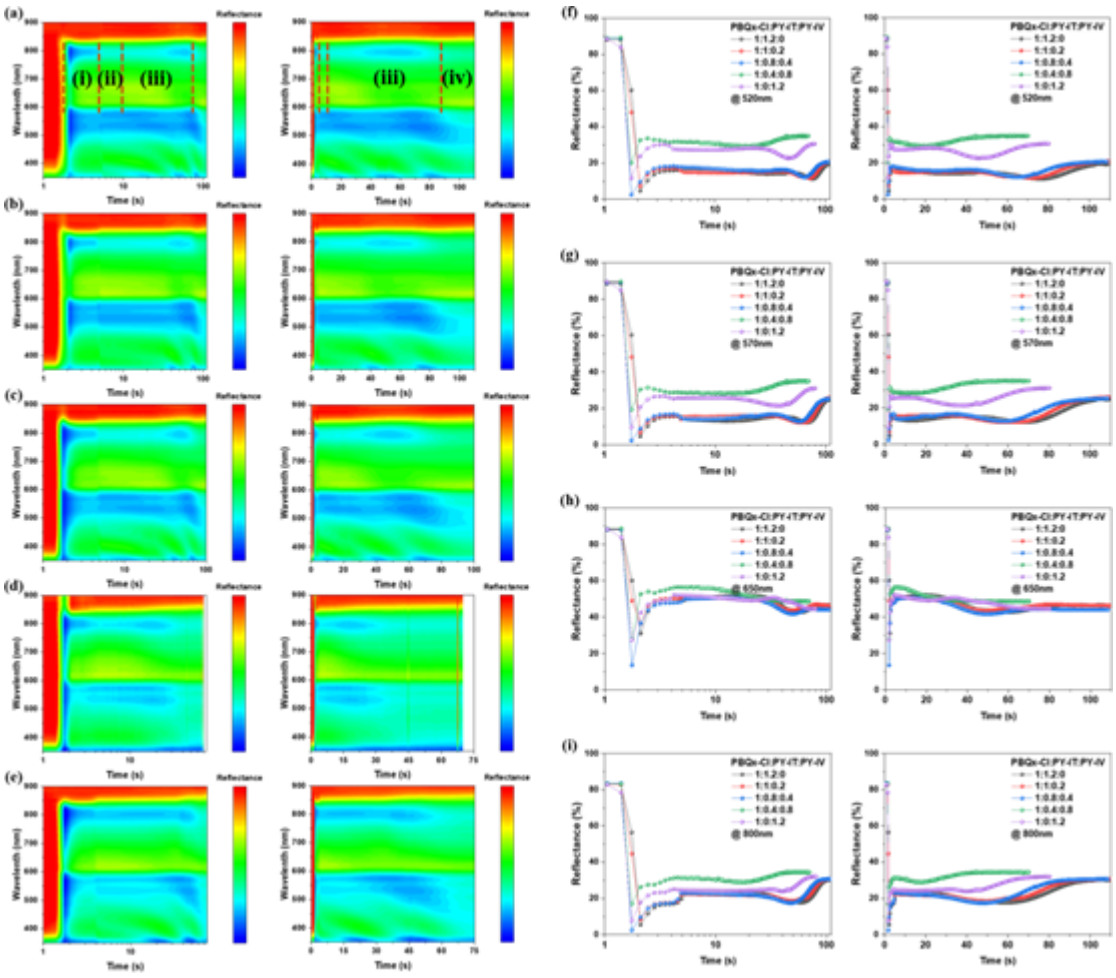

Figure 5. *In-situ* reflectance spectroscopy tracing of the spin coating process. The 2D contour maps in logarithmic (left) and linear (right) time scales of active layers in PBQx-TCl: PY-IT: PY-IV ternary films of all ratios: (a) 1:1.2:0, (b) 1:1:0.2, (c) 1:0.8:0.4, (d) 1:0.4:0.8, and (e) 1:0:1.2. The time-dependent reflectance of several wavelengths for all blends on logarithmic and linear time scales: (f) 520 nm, (g) 570 nm, (h) 650 nm, and (i) 800 nm.

Beyond the *ex-situ* morphology characterizations, the *in-situ* observations of the film formation process (spin coating and thermal annealing) should reveal the in-depth underlying mechanisms. This process was feasible for our research targets because of the strong temperature-dependent aggregation property of PBQx-TCl, the high boiling point of the main solvent toluene, and the incorporation of high proportion (2 *vol.*%) of solvent additive 1-chloronaphthalene (1-CN).[21,55,56] Hence, the *in-situ* reflectance spectra are measured in our study to gain more insights.[57-60] The 2D contour maps of time vs. wavelength vs. reflectance and extracted time vs. reflectance curves are presented in **Figure 5** (spin coating) and **Figure S18** (thermal annealing) on linear and logarithmic time scales, respectively. The spin coating possesses 4 typical stages based on the reflectance changing features: (i) removal of the main solvent (toluene) within the first several seconds; (ii) removal of toluene, but the removal of solvent additive (1-CN) did not start; (iii) removal of 1-CN for approximately 1 min; and (iv) completely solidified film. Considering this sequence, the logarithmic time scale presentation is beneficial for recognizing stage (i), whereas the linear one is useful in the comparison of stages (ii) and (iii) in different systems. The track on 520, 570, 650, and 800 nm of the entire liquid-to-solid phase transition represents the time-resolved characteristic change in 0-1 and 0-0 peaks of PBQx-TCl, the gap between donor and acceptor, and the main peak of acceptor materials. For those with a high proportion of PY-IT (>50%) in acceptors, stage (i) lasted for approximately 3.5 s, whereas in PY-IV-dominated systems, it lasted for approximately 2.8 s. Prolonged solidification could offer a chance for *J*-type pre-aggregates PBQx-TCl to turn to *H*-aggregates. This result may also be attributed to the better miscibility of PY-IT with PBQx-TCl: PY-IV, which can accomplish demixing with PBQx-TCl relatively quickly. Thus, the self-aggregation of PBQx-TCl is likely to be less affected by *J*-type pre-aggregates turning to *H*-aggregates and must exhibit 0-0 and 0-1 peak characteristics comparable to those of neat donor film. On the contrary, PY-IT can maintain the interaction with PBQx-TCl

for a longer time than that of PY-IV with PBQx-TCl during the liquid-to-solid phase transition, which helps tune the molecular arrangement and aggregation mode of PBQx-TCl. Consequently, the *H*-type aggregated PBQx-TCl may assume a larger proportion. After stage (ii), stage (iii) starts with changes in the secondary reflectance of donor and acceptor regions. Considering the late beginning and long duration of this stage, it is supposed to be caused by the removal of 1-CN (boiling point 260.27 ℃). Through a parallel comparison, the characteristic peak of PY-IV (@ 800nm in its binary film) changes before that of PY-IT (@ 800nm in its binary film), and before that of PBQx-TCl (from 500–580 nm in all systems). The end timing of alteration in donor reflectance is later than that for the acceptor. These results indicate PBQx-TCl has a tighter interaction with 1-CN than PY-IT/PY-IV does. Hence, the donor aggregation, in this case, is simultaneously modulated by acceptor materials and solvent additive, not only in stage (iii) but also in stage (i). As stage (iii) is complicated, hard to control, and time-consuming, the device fabrication limits the spin coating step to be 10 s in total, and then immediate thermal annealing upon fresh films for a stable and thorough 1-CN removal (110 ℃ hotplate). Note the liquid-to-solid processes of pristine films of PBQx-TCl, PY-IT and PY-IV are also tracked by the in-situ reflectance spectroscopy, which helps us precisely understanding the whole solidification process of blends. It can be seen in **Figure S17**, also with two types of time-scale presentations. The strong pre-aggregation property of PBQx-TCl is observed again, which exhibits only slight red-shifting after the removal of toluene, thereby determining its aggregation behavior must focus on blend's *in-situ* data. Both two polymer acceptors exhibit longer aggregation duration, thus confirmed to be able of tuning the aggregation of PBQx-TCl once they intertwine with each other (requiring good miscibility). In this scenario, PY-IT's stronger aggregation (wider color shifting range and longer duration) let it become more powerful in tuning PBQx-TCl than PY-IV is. As for the donor peak position tracing, donor peaks are at the 500 nm to 600 nm range without doubt, assuring the analysis for blend films is reliable.

The *in-situ* reflectance tracing of the entire annealing process similarly to that of the spin coating process is shown in **Figure S18**. Based on tracing @ 650 nm, the general light absorption ability of the active layers was promoted after the annealing process. Thermal annealing can remove 1-CN in a much shorter time (<5s) than taken by spin coating, ensuring fabrication reproducibility. The other three wavelength tracings showed the rise of reflectance after the drop, implying that enhancements in their aggregation occurred before the complete evaporation of 1-CN. The PY-IT-based binary film requires a longer duration for changes in reflectance than that required by PY-IV-rich films, consistent with the previous conclusion that PY-IT interacts relatively more strongly with 1-CN than exhibited by PY-IV. Variations in simple optical properties and subsequent stable reflectance imply that thermal annealing prevents the evolution of further complex (hard to control; thus, not desired) morphology. This finding agrees with the most optimal miscibility between PBQx-TCl and PY-IT leading to the smallest size of the pure phase (excessive aggregation is eliminated by immediate thermal annealing).

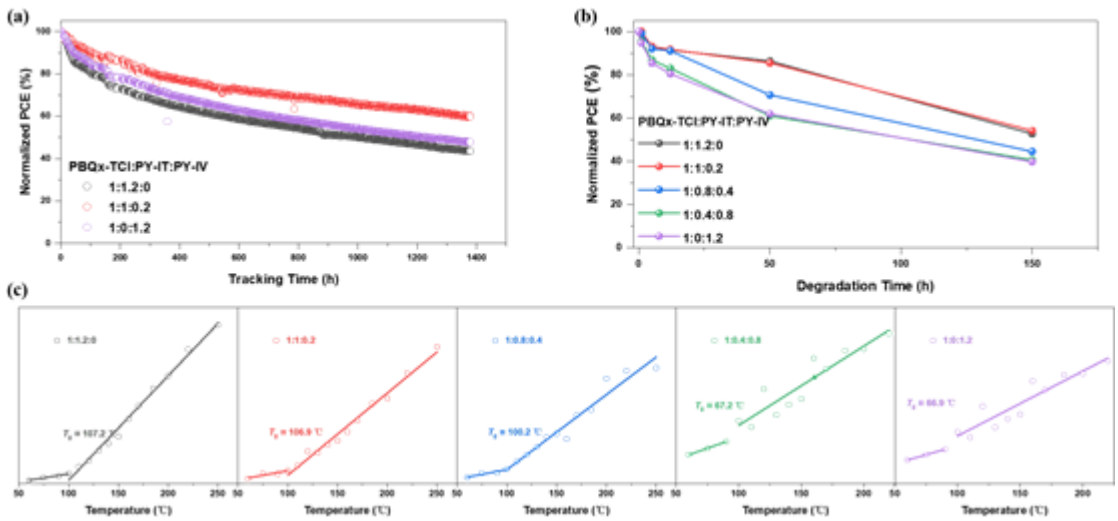

Figure 6. Maximal power point (MPP) tracking, thermal stability, and glass transition temperature (T_g) values of blend and neat films.

Finally, the device stabilities of binary controls and ternary targets under two typical conditions were measured. The MPP tracking curves of encapsulated devices in the ambient atmosphere are illustrated in **Figure 6a** (PCE) and **Figure S19** (V_{OC}, J_{SC}, and *FF*). The efficiency-optimized ternary cell exhibits improved operational stability with a T_{80} of 305 h and a T_{60} of 1359 h, outperforming those of PY-IT- (104 h, 551 h) and PY-IV- (161 h, 716 h) based binary controls. The main contribution of the promoted stability originates from the well-maintained *FF* of the ternary device. This factor is attributed to morphology optimization, wherein sizeable aggregates formed in the fibrillar network may be able to resist light-induced degradation in morphology. Thermal stabilities of all blends are also investigated by placing fresh devices on an 85 ℃ hotplate. Similarly, we present the efficiency variations in **Figure 6b**, and those of other parameters (V_{OC}, J_{SC}, and *FF*) are presented in **Figure S20**. Notably, the use of PY-IV is detrimental to thermal stability, as both faster decreases in V_{OC} and *FF* make the lifetime much shorter than with the application of PY-IT. Though morphology optimization was expected to improve thermal stability, the tendency was not alleviated. Subsequently, this is supposed to be primarily determined based on the intrinsic property of the material. Therefore, the glass transition temperatures (T_g) of the active layers were measured using a recently reported method.[61-63] The results are displayed in **Figure 6c**. The rising content of PY-IV gradually downshifted the T_g of the entire system from 107.2 ℃ to 66.9 ℃, leading to the poor thermal resistance of film morphology. The T_g value of 106.9 ℃ for the optimal ternary blend was at an acceptable level to maintain the stability of PY-IT-based binary control under external high-temperature stress. In contrast, the slopes of the two stages for the related systems also revealed that PY-IV was not thermally stable and that 1:0.4:0.8 and 1:0:1.2 films displayed steeper first-stage slopes and less distinct T_g points than in the others. Our study revealed improved

efficiency, promoted light stability, and well-maintained thermal stability of the designed ternary target.

Conclusion

In summary, structurally similar polymer acceptors PY-IT and PY-IV were found to exert different effects on the aggregation motif of the polymer donor PBQx-TCl. Various combinations of the two polymer acceptors and the polymer donor PBQx-TCl with different weight ratios were used to finely manipulate the general film morphology to pursue better PCE and desired stability. Relatively more amounts of *H*-aggregated PBQx-TCl with proper addition of PY-IV to extend the absorption edge were confirmed to be beneficial for improving J_{SC} and retaining V_{OC} in films. In addition, the slightly enlarged aggregates in the nano-fibrillar network (high pure phase size) contributed to increased *FF*. Time-scaled *in-situ* reflectance characterizations revealed that a prolonged process for the evaporation of the primary solvent could enhance *H*-aggregate formation in PBQx-TCl. The operational stability of the ternary target also improved owing to the optimized morphology. The low T_g of PY-IV-based films was confirmed, which explained the poor thermal stability of PY-IV-enriched systems. This work presents state-of-the-art PCE for all-PSCs with decent stabilities based on a ternary matrix construction while elucidating the underlying mechanism.

Author Contribution

Ruijie Ma: Conceptualization, Investigation, Formal Analysis, Methodology, Writing - Original Draft, Writing Review & Editing, Project Administration

Hongxiang Li: Investigation, Formal Analysis

Top Archie Dela Peña: Investigation, Formal Analysis, Writing - Original Draft

Xiyun Xie: Investigation

Patrick Wai-Keung Fong: Investigation

Qi Wei: Investigation

Cenqi Yan: Investigation

Jiaying Wu: Resources

Pei Cheng: Resources

Mingjie Li: Resources

Gang Li: Supervision, Conceptualization, Resources, Writing Review & Editing, Funding Acquisition

Acknowledgment

G. Li acknowledges the support from the Research Grants Council of Hong Kong (Project Nos. 15221320 and C5037-18G), RGC Senior Research Fellowship Scheme (SRFS2223-5S01), the Shenzhen Science and Technology Innovation Commission (JCYJ20200109105003940), the Hong Kong Polytechnic University Internal Research Funds: Sir Sze-yuen Chung Endowed Professorship Fund (8-8480), RISE (Q-CDA5), G-SAC5, 1-YW4C and Guangdong-Hong Kong-Macao Joint Laboratory for Photonic-Thermal-Electrical Energy Materials and Devices (GDSTC No. 2019B121205001). R. Ma gratefully acknowledges the support from PolyU Distinguished Postdoctoral

Fellowship (1-YW4C). Shanghai Beamline BL02U2 and BL16B1 are appreciated for GIWAXS and GISAXS data acquisition, respectively.

Reference

1. Z.-G. Zhang, Y. Li, *Angew. Chem. Int. Ed.* **2021**, 60, 4422.

2. Q. Fan, F. R. Lin, W. Ma, A. K. Y. Jen, *Sci. China Chem.* **2023**, 66, 615.

3. K. Zhou, K. Xian, L. Ye, *InfoMat* **2022**, 4, e12270.

4. Y. Kong, Y. Li, J. Yuan, L. Ding, *InfoMat* **2022**, 4, e12271.

5. Q. Fan, R. Ma, W. Su, Q. Zhu, Z. Luo, K. Chen, Y. Tang, F. R. Lin, Y. Li, H. Yan, C. Yang, A. K. Y. Jen, W. Ma, *Carbon Energy* **2023**, 5, e267.

6. Z. Zhang, Z. Li, P. Wang, H. Chen, K. Ma, Y. Zhang, T. Duan, C. Li, Z. Yao, B. Kan, X. Wan, Y. Chen, *Adv. Funct. Mater.* **2023**, n/a, 2214248.

7. Z. Genene, J.-W. Lee, S.-W. Lee, Q. Chen, Z. Tan, B. A. Abdulahi, D. Yu, T.-S. Kim, B. J. Kim, E. Wang, *Adv. Mater.* **2022**, 34, 2107361.

8. W. Zhang, C. Sun, I. Angunawela, L. Meng, S. Qin, L. Zhou, S. Li, H. Zhuo, G. Yang, Z.-G. Zhang, H. Ade, Y. Li, *Adv. Mater.* **2022**, 34, 2108749.

9. R. Ma, K. Zhou, Y. Sun, T. Liu, Y. Kan, Y. Xiao, T. A. Dela Peña, Y. Li, X. Zou, Z. Xing, Z. Luo, K. S. Wong, X. Lu, L. Ye, H. Yan, K. Gao, *Matter* **2022**, 5, 725.

10. Y. Liu, B. Liu, C.-Q. Ma, F. Huang, G. Feng, H. Chen, J. Hou, L. Yan, Q. Wei, Q. Luo, Q. Bao, W. Ma, W. Liu, W. Li, X. Wan, X. Hu, Y. Han, Y. Li, Y. Zhou, Y. Zou, Y. Chen, Y. Li, Y. Chen, Z. Tang, Z. Hu, Z.-G. Zhang, Z. Bo, *Sci. China Chem.* **2022**, 65, 224.

11. Y. Yang, W. Chen, L. Dou, W.-H. Chang, H.-S. Duan, B. Bob, G. Li, Y. Yang, *Nat. Photon.* **2015**, 9, 190.

12. H. Xia, Y. Zhang, W. Deng, K. Liu, X. Xia, C.-J. Su, U. S. Jeng, M. Zhang, J. Huang, J. Huang, C. Yan, W.-Y. Wong, X. Lu, W. Zhu, G. Li, *Adv. Mater.* **2022**, 34, 2107659.

13. J. Guo, X. Xia, B. Qiu, J. Zhang, S. Qin, X. Li, W. Lai, X. Lu, L. Meng, Z. Zhang, Y. Li, *Adv. Mater.* **2023**, n/a, 2211296.

14. T. Zhang, Y. Xu, H. Yao, J. Zhang, P. Bi, Z. Chen, J. Wang, Y. Cui, L. Ma, K. Xian, Z. Li, X. Hao, Z. Wei, J. Hou, *Energy Environ. Sci.* **2023**, 16, 1581.

15. R. Ma, Q. Fan, T. A. Dela Peña, B. Wu, H. Liu, Q. Wu, Q. Wei, J. Wu, X. Lu, M. Li, W. Ma, G. Li, *Adv. Mater.* **2023**, n/a, 2212275.

16. R. Sun, T. Wang, Q. Fan, M. Wu, X. Yang, X. Wu, Y. Yu, X. Xia, F. Cui, J. Wan, X. Lu, X. Hao, A. K. Y. Jen, E. Spiecker, J. Min, *Joule* **2023**, 7, 221.

17. T. Liu, K. Zhou, R. Ma, L. Zhang, C. Huang, Z. Luo, H. Zhu, S. Yao, C. Yang, B. Zou, L. Ye, *Aggregate* **2022**, n/a, e308.

18. X. Yang, R. Sun, Y. Wang, M. Chen, X. Xia, X. Lu, G. Lu, J. Min, *Adv. Mater.* **2022**, n/a, 2209350.

19. Y. Cai, C. Xie, Q. Li, C. Liu, J. Gao, M. H. Jee, J. Qiao, Y. Li, J. Song, X. Hao, H. Y. Woo, Z. Tang, Y. Zhou, C. Zhang, H. Huang, Y. Sun, *Adv. Mater.* **2023**, 35, 2208165.

20. L. Ma, Y. Cui, J. Zhang, K. Xian, Z. Chen, K. Zhou, T. Zhang, W. Wang, H. Yao, S. Zhang, X. Hao, L. Ye, J. Hou, *Adv. Mater.* **2023**, 35, 2208926.

21. R. Ma, C. Yan, P. W.-K. Fong, J. Yu, H. Liu, J. Yin, J. Huang, X. Lu, H. Yan, G. Li, *Energy Environ. Sci.* **2022**, 15, 2479.

22. Z. Li, Y. Liang, X. Qian, L. Ying, Y. Cao, *Chem. Eng. J.* **2022**, 446, 136877.

23. J. Fu, P. W. K. Fong, H. Liu, C.-S. Huang, X. Lu, S. Lu, M. Abdelsamie, T. Kodalle, C. M. Sutter-Fella, Y. Yang, G. Li, *Nat. Commun.* **2023**, 14, 1760.

24. Z. Luo, R. Ma, J. Yu, H. Liu, T. Liu, F. Ni, J. Hu, Y. Zou, A. Zeng, C.-J. Su, U. S. Jeng, X. Lu, F. Gao, C. Yang, H. Yan, *Nati. Sci. Rev.* **2022**, 9, nwac076.

25. L. Zhu, M. Zhang, J. Xu, C. Li, J. Yan, G. Zhou, W. Zhong, T. Hao, J. Song, X. Xue, Z. Zhou, R. Zeng, H. Zhu, C.-C. Chen, R. C. I. MacKenzie, Y. Zou, J. Nelson, Y. Zhang, Y. Sun, F. Liu, *Nat. Mater.* **2022**, 21, 656.

26. G. Li, V. Shrotriya, J. Huang, Y. Yao, T. Moriarty, K. Emery, Y. Yang, *Nat. Mater.* **2005**, 4, 864.

27. R. Ma, C. Yan, J. Yu, T. Liu, H. Liu, Y. Li, J. Chen, Z. Luo, B. Tang, X. Lu, G. Li, H. Yan, *ACS Energy Lett.* **2022**, 7, 2547.

28. T. Chen, S. Li, Y. Li, Z. Chen, H. Wu, Y. Lin, Y. Gao, M. Wang, G. Ding, J. Min, Z. Ma, H. Zhu, L. Zuo, H. Chen, *Adv. Mater.* **2023**, n/a, 2300400.

29. X. Xu, W. Jing, H. Meng, Y. Guo, L. Yu, R. Li, Q. Peng, *Adv. Mater.* **2023**, 35, 2208997.

30. Z. Zheng, J. Wang, P. Bi, J. Ren, Y. Wang, Y. Yang, X. Liu, S. Zhang, J. Hou, *Joule* **2022**, 6, 171.

31. J. Wang, Z. Zheng, P. Bi, Z. Chen, Y. Wang, X. Liu, S. Zhang, X. Hao, M. Zhang, Y. Li, J. Hou, *Nati. Sci. Rev.* **2023**, DOI: 10.1093/nsr/nwad085nwad085.

32. Q. Fan, R. Ma, Z. Bi, X. Liao, B. Wu, S. Zhang, W. Su, J. Fang, C. Zhao, C. Yan, K. Chen, Y. Li, C. Gao, G. Li, W. Ma, *Adv. Funct. Mater.* **2023**, 33, 2211385.

33. Y. Wei, Z. Chen, G. Lu, N. Yu, C. Li, J. Gao, X. Gu, X. Hao, G. Lu, Z. Tang, J. Zhang, Z. Wei, X. Zhang, H. Huang, *Adv. Mater.* **2022**, 34, 2204718.

34. Y. Xu, Y. Cui, H. Yao, T. Zhang, J. Zhang, L. Ma, J. Wang, Z. Wei, J. Hou, *Adv. Mater.* **2021**, 33, 2101090.

35. D. Li, Y. Huang, R. Ma, H. Liu, Q. Liang, Y. Han, Z. Ren, K. Liu, P. W.-K. Fong, Z. Zhang, Q. Lian, X. Lu, C. Cheng, G. Li, *Adv. Energy Mater.* **2023**, n/a, 2204247.

36. Z. Luo, T. Liu, R. Ma, Y. Xiao, L. Zhan, G. Zhang, H. Sun, F. Ni, G. Chai, J. Wang, C. Zhong, Y. Zou, X. Guo, X. Lu, H. Chen, H. Yan, C. Yang, *Adv. Mater.* **2020**, 32, 2005942.

37. H. Yu, Y. Wang, H. K. Kim, X. Wu, Y. Li, Z. Yao, M. Pan, X. Zou, J. Zhang, S. Chen, D. Zhao, F. Huang, X. Lu, Z. Zhu, H. Yan, *Adv. Mater.* **2022**, 34, 2200361.

38. X. Xiong, X. Xue, M. Zhang, T. Hao, Z. Han, Y. Sun, Y. Zhang, F. Liu, S. Pei, L. Zhu, *ACS Energy Lett.* **2021**, 6, 3582.

39. J. Fu, P. W. K. Fong, H. Liu, C.-S. Huang, X. Lu, S. Lu, M. Abdelsamie, T. Kodalle, C. M. Sutter-Fella, Y. Yang, G. Li, *Nat. Commun.* **2023**, 14, 1760.

40. H. Liang, H. Chen, P. Wang, Y. Zhu, Y. Zhang, W. Feng, K. Ma, Y. Lin, Z. Ma, G. Long, C. Li, B. Kan, Z. Yao, H. Zhang, X. Wan, Y. Chen, *Adv. Funct. Mater.* **2023**, n/a, 2301573.

41. W. Zou, C. Han, X. Zhang, J. Qiao, J. Yu, H. Xu, H. Gao, Y. Sun, Y. Kan, X. Hao, G. Lu, Y. Yang, K. Gao, *Adv. Energy Mater.* **2023**, n/a, 2300784.

42. R. Ma, Y. Tao, Y. Chen, T. Liu, Z. Luo, Y. Guo, Y. Xiao, J. Fang, G. Zhang, X. Li, X. Guo, Y. Yi, M. Zhang, X. Lu, Y. Li, H. Yan, *Sci. China Chem.* **2021**, 64, 581.

43. K. Xian, S. Zhang, Y. Xu, J. Liu, K. Zhou, Z. Peng, M. Li, W. Zhao, Y. Chen, Z. Fei, J. Hou, Y. Geng, L. Ye, *Sci. China Chem.* **2023**, 66, 202.

44. B. Pang, C. Liao, X. Xu, L. Yu, R. Li, Q. Peng, *Adv. Mater.* **2023**, n/a, 2300631.

45. T. Chen, S. Li, Y. Li, Z. Chen, H. Wu, Y. Lin, Y. Gao, M. Wang, G. Ding, J. Min, Z. Ma, H. Zhu, L. Zuo, H. Chen, *Adv. Mater.* **2023**, n/a, 2300400.

46. T. A. Dela Peña, J. I. Khan, N. Chaturvedi, R. Ma, Z. Xing, J. Gorenflot, A. Sharma, F. L. Ng, D. Baran, H. Yan, F. Laquai, K. S. Wong, *ACS Energy Lett.* **2021**, 6, 3408.

47. S. Li, C. He, T. Chen, J. Zheng, R. Sun, J. Fang, Y. Chen, Y. Pan, K. Yan, C.-Z. Li, M. Shi, L. Zuo, C.-Q. Ma, J. Min, Y. Liu, H. Chen, *Energy Environ. Sci.* **2023**, DOI: 10.1039/D3EE00630A.

48. D. Baran, R. S. Ashraf, D. A. Hanifi, M. Abdelsamie, N. Gasparini, J. A. Röhr, S. Holliday, A. Wadsworth, S. Lockett, M. Neophytou, C. J. M. Emmott, J. Nelson, C. J. Brabec, A. Amassian, A. Salleo, T. Kirchartz, J. R. Durrant, I. McCulloch, *Nat. Mater.* **2017**, 16, 363.

49. S.-i. Natsuda, T. Saito, R. Shirouchi, Y. Sakamoto, T. Takeyama, Y. Tamai, H. Ohkita, *Energy Environ. Sci.* **2022**, 15, 1545.

50. S. Albrecht, K. Vandewal, J. R. Tumbleston, F. S. U. Fischer, J. D. Douglas, J. M. J. Fréchet, S. Ludwigs, H. Ade, A. Salleo, D. Neher, *Adv. Mater.* **2014**, 26, 2533.

51. Y. Xiao, J. Yuan, G. Zhou, K. C. Ngan, X. Xia, J. Zhu, Y. Zou, N. Zhao, X. Zhan, X. Lu, *J. Mater. Chem. A* **2021**, 9, 17030.

52. X. Jiang, P. Chotard, K. Luo, F. Eckmann, S. Tu, M. A. Reus, S. Yin, J. Reitenbach, C. L. Weindl, M. Schwartzkopf, S. V. Roth, P. Müller-Buschbaum, *Adv. Energy Mater.* **2022**, 12, 2103977.

53. D. Li, N. Deng, Y. Fu, C. Guo, B. Zhou, L. Wang, J. Zhou, D. Liu, W. Li, K. Wang, Y. Sun, T. Wang, *Adv. Mater.* **2023**, 35, 2208211.

54. R. Ma, X. Jiang, J. Fu, T. Zhu, C. Yan, K. Wu, P. Müller-Buschbaum, G. Li, *Energy Environ. Sci.* **2023**, 16, 2316.

55. P. Bi, J. Wang, Y. Cui, J. Zhang, T. Zhang, Z. Chen, J. Qiao, J. Dai, S. Zhang, X. Hao, Z. Wei, J. Hou, *Adv. Mater.* **2023**, 35, 2210865.

56. J. Wang, Y. Wang, P. Bi, Z. Chen, J. Qiao, J. Li, W. Wang, Z. Zheng, S. Zhang, X. Hao, J. Hou, *Adv. Mater.* **2023**, n/a, 2301583.

57. Y. Liu, Y. Jin, Y. Wu, Y. Zhong, *Journal of Materials Chemistry C* **2022**, 10, 13646.

58. Z. Shen, J. Yu, G. Lu, K. Wu, Q. Wang, L. Bu, X. Liu, Y. Zhu, G. Lu, *Energy Environ. Sci.* **2023**, DOI: 10.1039/D3EE00090G.

59. L. Chen, J. Yi, R. Ma, L. Ding, T. A. Dela Peña, H. Liu, J. Chen, C. Zhang, C. Zhao, W. Lu, Q. Wei, B. Zhao, H. Hu, J. Wu, Z. Ma, X. Lu, M. Li, G. Zhang, G. Li, H. Yan, *Adv. Mater.* **2023**, n/a, 2301231.

60. Y.-F. Shen, H. Zhang, J. Zhang, C. Tian, Y. Shi, D. Qiu, Z. Zhang, K. Lu, Z. Wei, *Adv. Mater.* **2023**, 35, 2209030.

61. S. E. Root, M. A. Alkhadra, D. Rodriquez, A. D. Printz, D. J. Lipomi, *Chem. Mater.* **2017**, 29, 2646.

62. Y. Qin, N. Balar, Z. Peng, A. Gadisa, I. Angunawela, A. Bagui, S. Kashani, J. Hou, H. Ade, *Joule* **2021**, 5, 2129.

63. C. Zhang, M. Zhang, Q. Zhou, S. Chen, S. Kim, J. Yao, Z. Zhang, Y. Bai, Q. Chen, B. Chang, H. Fu, L. Xue, H. Wang, C. Yang, Z.-G. Zhang, *Adv. Funct. Mater.* **2023**, 33, 2214392.

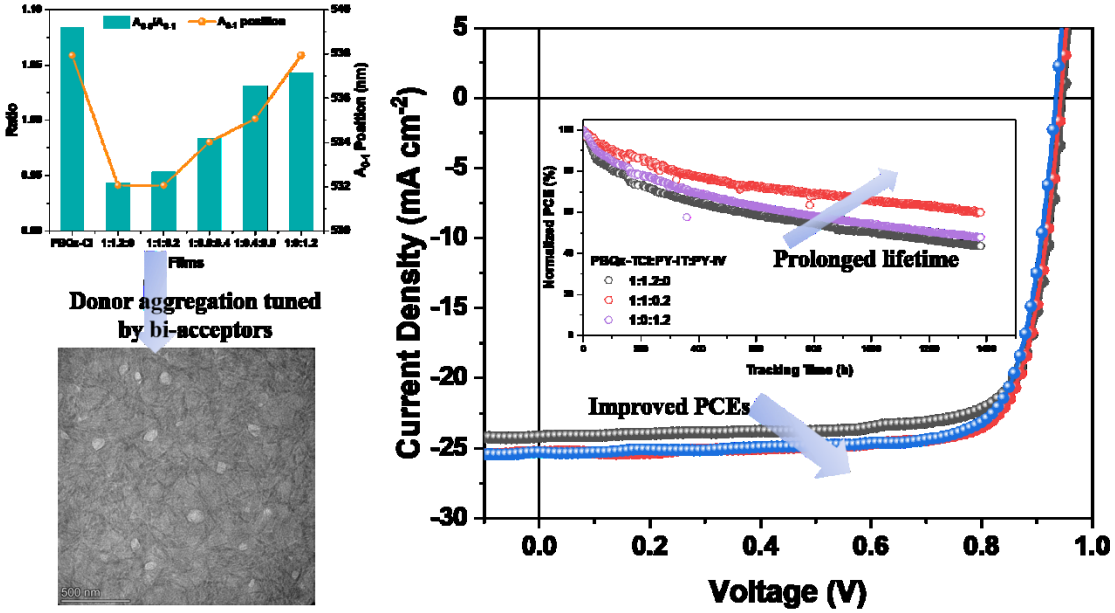

Dual-acceptor strategy in all-polymer photovoltaic blend pushes the efficiencies up to 18.81%, with decent changes in MPP tracked and thermal stress applied stability tests, where a new phenomenon that donor aggregation modulated by acceptor component is focused on and carefully analyzed. The experience of ternary blend design from here is supposed to be instructive for other OPV systems, too.